

TABLE III  
QUANTITATIVE ANALYSIS OF THE IMAGES

(a)	Scene1	Scene2	Scene3	Scene4	Scene5	Scene6
Striped						
Detector 1	19.261	23.283	25.674	28.382	86.751	208.283
Detector 2	15.935	19.805	21.892	24.637	84.885	209.311
Detector 3	19.131	23.022	25.783	28.546	86.616	207.876
Detector 4	12.435	16.544	18.305	21.364	83.289	212.325

(b)	Scene1	Scene3	Scene3	Scene4	Scene5	Scene6
Destriped						
Detector 1	16.261	20.283	22.674	25.382	84.751	209.283
Detector 2	16.935	20.805	22.892	25.637	84.885	208.311
Detector 3	16.131	20.022	22.783	25.546	84.616	208.897
Detector 4	16.435	20.544	22.305	25.364	84.289	208.663

TABLE IV  
ESTIMATION OF THE EXTENT OF DESTRIPIING ON THE RAW IMAGES

(a)	Scene1	Scene2	Scene3	Scene4	Scene5	Scene6
Stripe <sub>max-min</sub>	7.608	6.827	6.739	7.319	7.479	7.182
Destripe <sub>max-min</sub>	0.863	0.805	0.783	0.523	0.587	0.273

(b)	Scene1	Scene2	Scene3	Scene4	Scene5	Scene6
S <sub>stddev</sub>	3.614	3.228	3.371	3.509	3.566	3.427
D <sub>stddev</sub>	0.436	0.353	0.337	0.216	0.256	0.132

analyzed, and Table III(a) shows raw DN levels from the actual striped scene data, whereas Table III(b) shows the DN levels after destriping the images. It can be clearly seen that there is a large variation in the detector response (Scene 1: 19.261, 15.935, 19.131, 12.435 DN), and the mismatch of the detectors causes striping to the scenes. After destriping the images, using the calibration curves derived from (1), the mismatch between the detectors had been significantly reduced (Scene 1: 16.261, 16.935, 16.131, 16.435 DN). Table IV gives a quantitative estimation of the extent of destriping. The data from Table III were used to find the maximum variation between detectors (Scene 1: 7.608 DN for the striped image and 0.863 DN after destriping) and the standard deviation (Scene 1: 3.614 DN for the striped image and 0.436 DN after destriping) of the detectors in a scan. Regression equations used for destriping the images hold well throughout the lifetime and over the complete dynamic range of the instrument.

## V. CONCLUSIONS

An algorithm has been developed that significantly reduces striping in images from Landsat-4/5 Band-6. DC restore circuitry implemented in Band-6 does not appear to function as it had been designed to. The data acquired during the calibration shutter interval is virtually useless for correction of the individual responses of the four detectors in Band-6. It was observed and statistically quantified that there is a very significant correlation between relative detector responses over the dynamic range and through the lifetime of the instrument. One can perform "relative" calibration of the detectors based on a static set of calibration curves since the relative responses of the detectors to one another are extremely stable. The results show that destriping can be easily performed and there is a consistent characterization of the L-4/5 response, which suggests potential for performing meaningful absolute calibration. Future work is possible to accomplish absolute calibration by using Band 6 specific Landsat ground truth data and relating the absolute response of the instrument to scene input radiance.

## ACKNOWLEDGMENT

The authors would like to thank J. Barker and B. Markham of Goddard Space Flight Center, Greenbelt, MD, and R. Morfitt of EROS Data Center, Sioux City, SD, for information and feedback.

## REFERENCES

- [1] B. L. Markham and L. R. Barker, "Spectral characterization of the LANDSAT Thematic Mapper sensors," *Int. J. Remote Sensing*, vol. 6, pp. 697–716, 1985.
- [2] K. Thome, B. Markham, J. Barker, P. Slater, and S. Biggar, "Radiometric calibration of Landsat," *Photogramm. Eng. Remote Sensing*, vol. 63, pp. 853–858, 1997.
- [3] R. R. Turtle, "ETM+ Band 6 calibration report," *Raytheon, Santa Barbara Remote Sensing*, Jan. 7, 1999.
- [4] R. A. Schowengerdt, *Remote Sensing: Models and Methods for Image Processing*, 2nd ed. New York: Academic, 1997.

## Haze Detection and Removal in High Resolution Satellite Image With Wavelet Analysis

Yong Du, Bert Guindon, and Josef Cihlar

**Abstract**—A procedure for haze detection and removal from high-resolution satellite images using wavelet analysis (HAWAT) has been developed. It involves the analysis of the low spatial frequency information content of a scene. The image contaminated by haze is decomposed into different spatial layers with wavelet transforms. Although haze is distributed in the lower frequency layer, this layer may also contain a component of land cover that is spatially and temporally relatively stable. A haze-free reference image of the same area is used to characterize land cover. The component of the characterized land cover is then subtracted with wavelet analysis. The residual wavelet coefficients are used to construct a spatially varying mask for subsequent haze detection and removal. After smoothing, the mask is subtracted from the contaminated image to obtain a corrected image with haze-off characteristics. Both visual inspection and statistical accuracy assessment show that the haze calibration is valid and robust.

**Index Terms**—Haze detection and removal, multiple spectral scanner (MSS), satellite high resolution image.

## I. INTRODUCTION

SOLAR radiation used in satellite remote sensing must pass through the Earth's atmosphere. During propagation, this radiation interacts with the atmosphere, generating a variety of effects upon the resulting satellite image that must subsequently be accounted for through atmospheric corrections [23], [5], [9]. Some atmospheric effects, such as cloud, block almost all radiation in the visible and infrared spectral regions. Others partly obscure the ground-reflected radiation leaving an underlying ground information component in contaminated form. "Haze" is an example of this latter effect. Haze is a commonly used term in image analysis, referring to a set of atmospheric effects that

Manuscript received November 2, 2000; revised August 15, 2001.

Y. Du is with Intermap Technologies, Inc., Ottawa, ON, K2E 1A2 Canada (e-mail: Yong.du@ccrs.nrcan.gc.ca).

B. Guindon and J. Cihlar are with the Canada Centre for Remote Sensing, Ottawa, ON, K1A 0Y7 Canada.

Publisher Item Identifier S 0196-2892(01)01408-5.

reduce image contrast. In general, the impact of haze is evident when viewing images in blue or green parts of the electromagnetic spectrum. At those wavelengths, it is generally an additive radiometric effect and varies spatially, with the resulting satellite image typically exhibiting the underlying ground cover in a diffused pattern. It is imperative that haze be removed prior to scene analysis.

Several different atmospheric scattering or “haze” detection and removal techniques have been reported in the literature. They include simple dark-object subtraction [24], [4], image-based dark target approaches [22], complex atmospheric radiative transfer (RT) modeling [10], [19], [21], [15], [16], and corrections using a) multitemporal or multichannel images [3], [11], [12], b) *in situ* ground data [1], [14], or c) nominally invariant targets [17].

A major disadvantage of atmospheric RT models is that they require coincident auxiliary information, such as path radiance and/or atmospheric transmission determined at several locations within the image coverage during the satellite overpass. While the use of *in situ* information might be the most accurate in terms of correcting for atmospheric haze effects, most users must work with remotely sensed data that have already been collected and therefore, do not have access to such information. In particular, extensive and potentially very valuable Landsat data have been collected over the last 30 years, in virtually all cases without accompanying information on atmospheric transmittance. Some techniques use within-scene reference targets. In particular, the simple dark-object subtraction mentioned above is robust requires only information contained in the image data. However, as it is usually implemented, this method can provide only point estimates and its use usually assumes a constant haze value throughout the entire image. It also ignores multiplicative effects, and therefore is of limited use in modeling spatially varying haze over larger scenes.

The present paper focuses on the spatial information content of high-resolution satellite images using wavelet transform analysis techniques. It takes advantage of haze distribution typically being distributed with spatially lower frequency. Although the distribution of land cover also contains some components of low frequency, the latter is comparatively stable in the temporal sense and tends to exhibit distinct texture. If the land cover spatial component can be modeled and removed from the overall low frequency content of an image, the remaining haze contribution can be subtracted from the image to obtain an estimated haze-free rendition. An important potential advantage of this method is its ability to account for complex spatial variation of haze within a scene, thus allowing use of algorithms that depend on image texture or radiometry. Experimental results are presented for the case of a contaminated Landsat multiple spectral scanner (MSS) subscene (path 24 row 29) acquired in 1991. This image was corrected successfully by using wavelet analysis with the aid of a haze free reference image from 1986.

## II. HAZE AND HIGH RESOLUTION SATELLITE IMAGE

Haze is mainly generated by atmospheric scattering, which is commonly modeled using *Mie* theory. This type of scattering is caused by larger particles present in the atmosphere, including dust, smoke, pollen, and water droplets. *Mie* scattering is selective and its effects are wavelength dependent. Under some environmental conditions, more particles occur in the atmosphere, resulting in visually detectable haze, especially at the shorter wavelengths. The spatial distribution of the particles depends on weather conditions (wind, water vapor content, etc.) and the location of dust sources. In a hazy image, a fuzzy outline of land cover usually remains. Because haze propagates through atmospheric disturbances such as wind and convection, the spatial variation of its distribution will be slower (on the scale of km) than for land cover which changes mainly at higher frequencies. Therefore, it can be

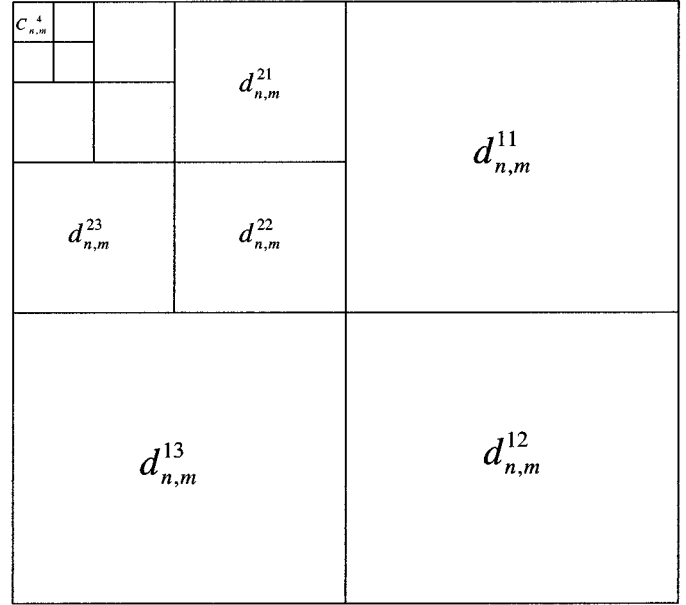


Fig. 1. Standard orthonormal decomposition with four levels.

assumed that in the case of a hazy image the low spatial frequency component is dominated by haze, while the high-frequency components reflect the effect of land cover. This spatial scale segregation will be most acute in the case of satellite images with a spatial resolution of less than 100 m, e.g., the Landsat, SPOT, and IRS sensor payloads. Finally, typical haze contamination will be most pronounced in the visible bands and is weaker or visually undetectable in the near- or shortwave-infrared parts of the spectrum.

Because of the frequency dependence of haze effects and wavelet analysis, a new and solid mathematical tool represents a potentially powerful approach. The critical problems in wavelet-based haze correction are the decomposition of the satellite image into spatially different frequency layers and the extraction of the spatially lower frequency component caused by haze.

## III. WAVELETS

Wavelets were developed in signal processing theory to help model temporal signal variability, which represents the details of a signal as an alternative manner to convenient temporal and Fourier descriptions. Wavelets can be described for two-dimensional (2-D) signals, of which satellite images are a special case.

For the one-dimensional (1-D) case, assume  $\{V_j\}_{j \in \mathbb{Z}}$  is a multiresolution analysis,  $\Phi(x)$  is a scale function or associated function, and  $\Psi(x)$  is a wavelet function. Some properties of  $\Psi(x)$  and  $\Phi(x)$  are as follows.

The integral of  $\Psi(x)$  is zero, ( $\int \psi(x) dx = 0$ ), and  $\Psi(x)$  is used to define the details (higher frequencies). The integral of  $\Phi(x)$  is 1, ( $\int \Phi(x) dx = 1$ ), and  $\Phi(x)$  is used to define the approximations (lower frequencies). A set of wavelet basis functions  $\{\Psi_{a,b}(x)\}$  can be generated by translating and scaling the basic wavelet  $\Psi(x)$  as

$$\psi_{a,b}(x) = \frac{1}{\sqrt{a}} \psi\left(\frac{x-b}{a}\right) \quad (1)$$

where  $a > 0$  and both  $a$  and  $b$  are real numbers. The variable  $a$  reflects the scale (width) of a particular basis function, while  $b$  specifying its translated position along the  $x$ -axis.

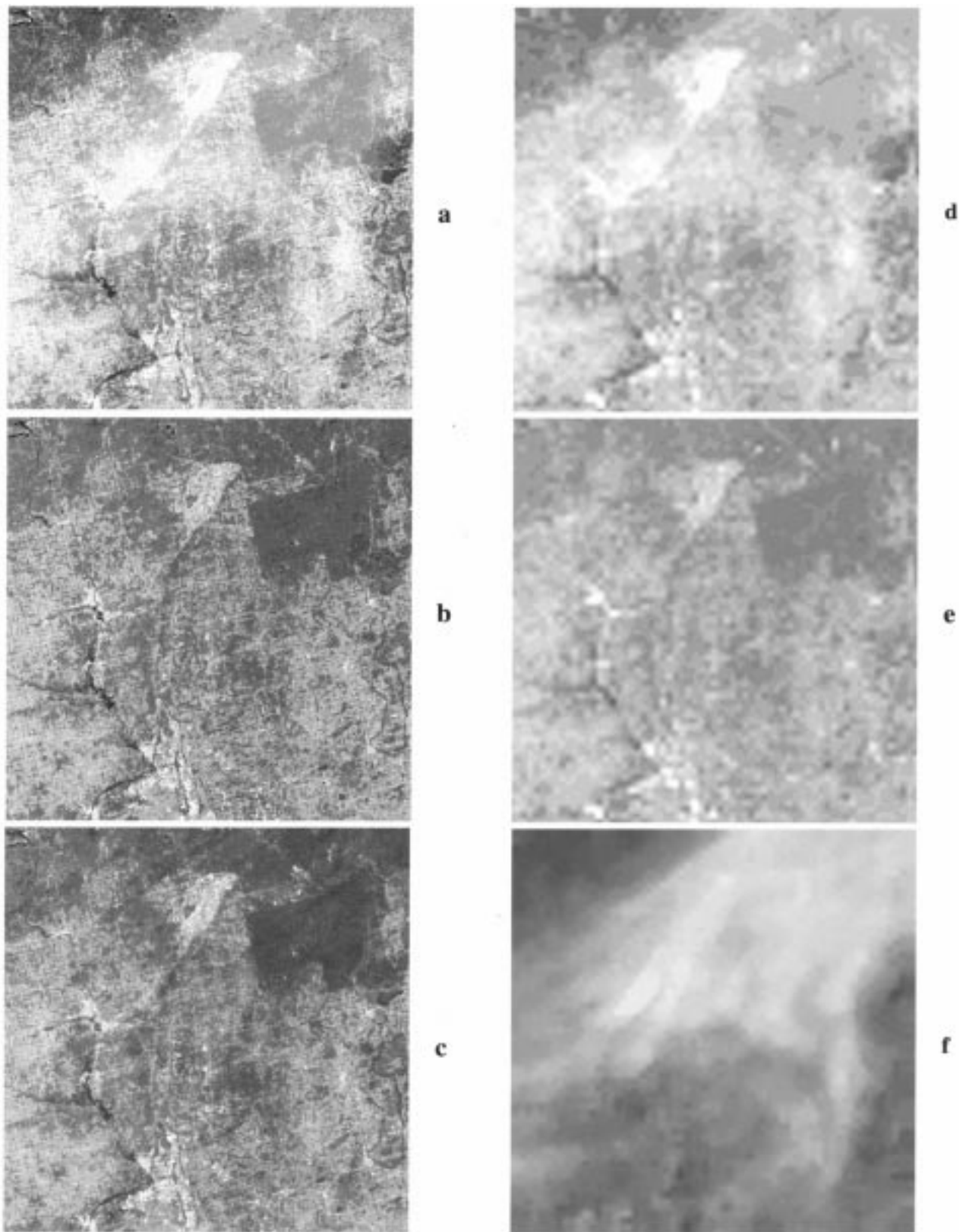


Fig. 2. Haze detection and removal with wavelet analysis in band 1 (in gray levels). (a) Original hazy image of band 1, 1991; (b) haze-free image of band 1, 1986; (c) corrected image haze off with wavelet analysis, 1991; (d) approximation of hazy image, 1991, with db4, level 5; (e) approximation of haze free image with db4, level 5; and (f) calculated haze distribution of original image.

For the 2-D case, the discrete wavelet transform, based on tensor products, the two-dimension orthonormal wavelet bases and the

multi-resolution orthonormal wavelet decomposition of a digital image  $\{C_{n,m}^0\}_{n,m \in \mathbb{Z}}$  can be formulated. If the total number of

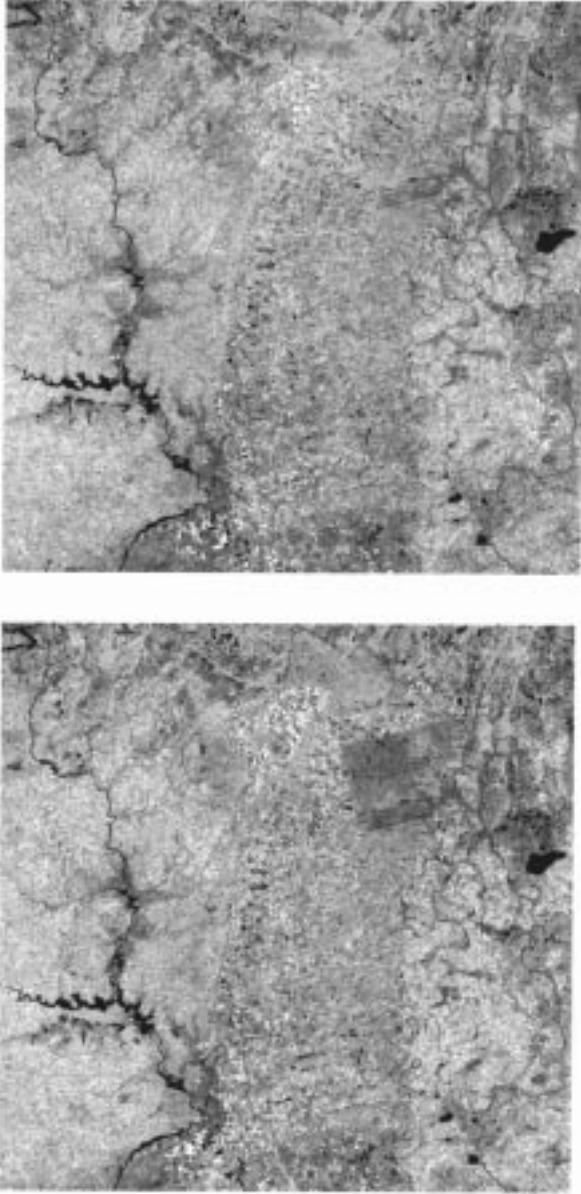


Fig. 3. Image 1991 and image 1986 in band 3 (in gray levels). (a) Original hazy image of band 3, 1991 and (b) original haze free image of band 3, 1986.

decomposition levels is  $N$ , the formulae of decomposition of level  $k$  are

$$\begin{aligned}
 C_{n,m}^k &= \sum_{j,l \in \mathbb{Z}} \bar{h}_{j-2n} \bar{h}_{l-2m} C_{j,l}^{k-1} \\
 d_{n,m}^{k1} &= \sum_{j,l \in \mathbb{Z}} \bar{h}_{j-2n} \bar{g}_{l-2m} C_{j,l}^{k-1} \\
 d_{n,m}^{k2} &= \sum_{j,l \in \mathbb{Z}} \bar{g}_{j-2n} \bar{h}_{l-2m} C_{j,l}^{k-1} \\
 d_{n,m}^{k3} &= \sum_{j,l \in \mathbb{Z}} \bar{g}_{j-2n} \bar{g}_{l-2m} C_{j,l}^{k-1}. \quad k = 1, 2, \dots, N \quad (2)
 \end{aligned}$$

where  $\{h_k\}_{k \in \mathbb{Z}}$  are orthonormal wavelet filter coefficients ( $g_k = (-1)^{k-1} \bar{h}_{1-k}$ ), and  $\{d_{n,m}^{k1}\}$  is the horizontal detail of  $k$  level,  $\{d_{n,m}^{k2}\}$  the vertical detail,  $\{d_{n,m}^{k3}\}$  the diagonal detail, and  $\{C_{n,m}^k\}$  the low frequencies.

Fig. 1 represents an example of orthonormal wavelet decomposition of an image with four levels. By the wavelet transform, an image can be decomposed into a multiresolution frame in which every portion has distinct frequency and spatial properties.

Unlike conventional techniques such as Fourier transform, wavelet decomposition produces a family of hierarchically organized decompositions. The selection of a suitable level of the hierarchy for an application such as haze characterization will depend on the image and human expertise. There are different types of wavelet families whose qualities vary according to several criteria. The selection of a wavelet family for image decomposition will hinge on the properties of the wavelet family and the characteristics of image. We have selected the Daubechies wavelet family ( $dbN$ ), a commonly used family of continuous scaling functions and wavelets [7]. The  $dbN$  includes Haar wavelet  $db1$ , the simplest wavelet imaginable and certainly one of the first studied. For  $dbN$ , the support length of  $\Psi$  and  $\Phi$  is  $2N - 1$ , where  $N$  is the number of vanishing moments of  $\Psi$ .

#### IV. WAVELET DECOMPOSITION OF AN IMAGE FOR THE DETECTION AND REMOVAL OF HAZE

Two co-registered MSS images [path 24 row 29, acquisition dates, August 16, 1986 (MSS-86), August 14, 1991 (MSS-91)] were used in this study. They constitute part of the North American Landscape Characterization (NALC) data set [13]. The 1991 image (a) is contaminated by haze [Fig. 2(a)], while the 1986 image (b) is visually much clearer and appears to be haze-free [Fig. 2(b)]. We assumed that the 1986 image is haze-free for the purposes of this paper. Two co-registered subscenes ( $2048 \times 2048$  pixels) were selected for the study. For convenience, these will be referenced as image A (1991) and B (1986), respectively. It should be noted that all images and computations are based on the recorded digital numbers.

The various orders of Daubechies wavelet have different properties, including regularity and asymmetry [8]. In the decomposition of the images for this study, the properties of the different order of Daubechies wavelet would not be the most important factor as the level of decomposition. Therefore, we chose the  $db4$ , which has proper length of filter and results in a reasonable haze distribution visually. Wavelet transforms also produce some border distortion during the decomposition of the image, thereby contaminating a narrow strip along the edge of the entire image. In this study, the border distortion eliminated by extending the size of image with periodic symmetry method [6]. The level of decomposition for wavelet analysis determines what spatial scale of land cover should be considered relatively stable, higher levels of decomposition being associated with larger spatial scales. If the level of decomposition is too low (i.e., higher spatial frequency level), finer land cover detail will be lost after the haze-off correction. The  $db4$  level 5 has been selected as a compromise. In the case of level 4, some land cover detail is lost in the haze-off correction, based on visual inspection, while level 6 is too coarse to provide a proper rendition of the complexities of the haze distribution that can be perceived in Fig. 2(a).

In applying the procedure, the image A (MSS-91, Band 1) has been decomposed with  $db4$  to level 5. When this approximation is reconstructed with the scaling component of level 5, only the lower frequency layer of the image is left and the higher frequency distribution is filtered out [Fig. 2(d)]. Obviously, this distribution includes the spatially lower frequency characteristics of both land cover and haze.

We assume that the spatially lower frequency characteristics of the land cover are relatively stable over time. If a reference haze-free image is available, the distribution of its land cover characteristics can be obtained by the same processing. We chose image B (MSS-86, band 1)

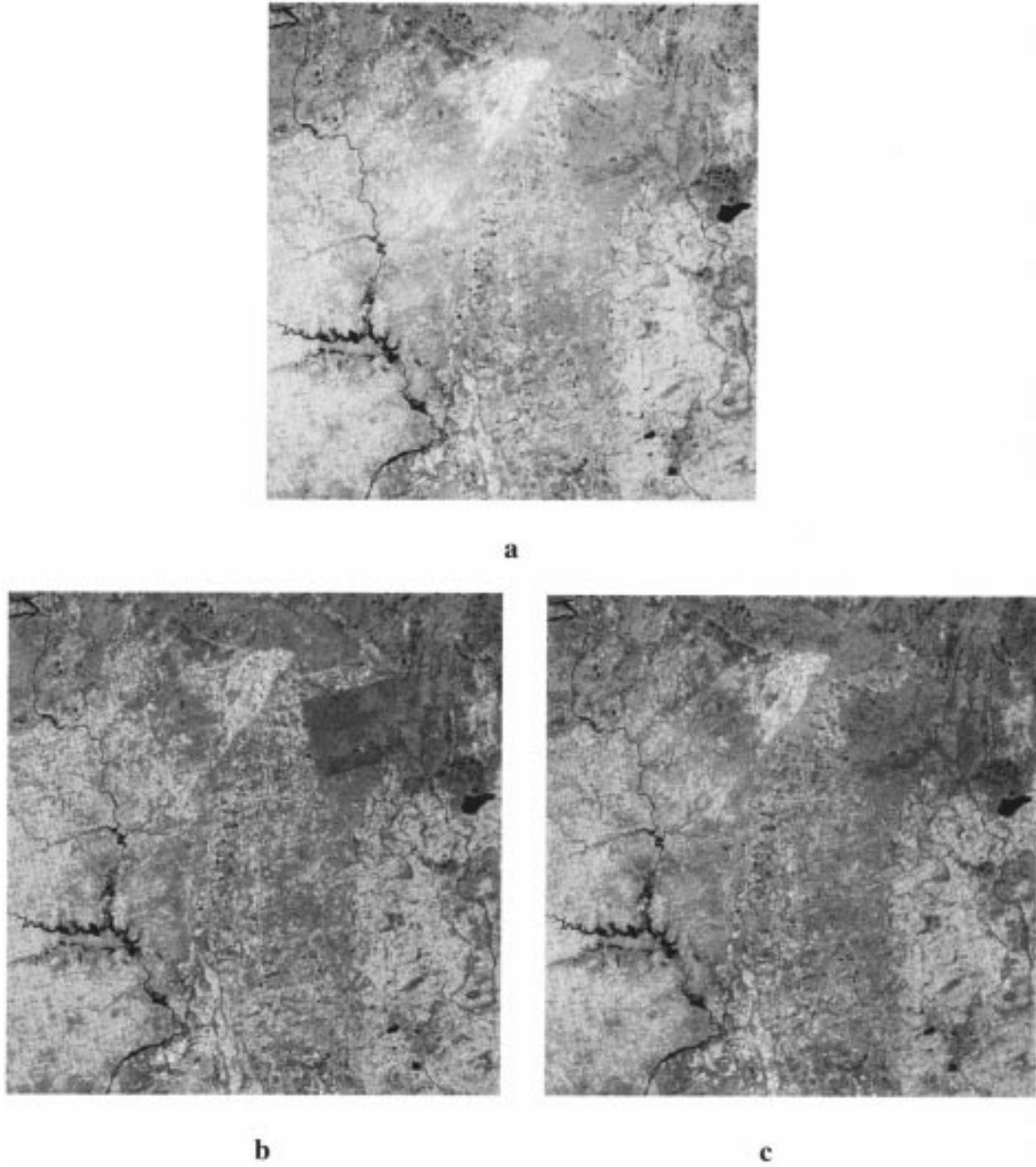


Fig. 4. Color composition images, Band 1 = blue, Band 2 = red, band 3 = green (in gray levels). (a) Original hazy MSS image, 1991; (b) haze-free MSS image, 1986; and (c) corrected haze off MSS, 1991.

as the reference image. Fig. 2(e) shows the reconstructed approximation of image B with the scaling component of *db4* level 5. To extract the land cover lower frequency characteristics from image A, we processed the scaling components of image A with that of image B to get the approximation components of haze,  $cA_h$

$$cA_h = \begin{cases} cA - cB, & \text{if } cA \geq cB \\ 0, & \text{if } cA < cB \end{cases} \quad (3)$$

where  $cA$  is the level 5 approximation coefficient matrix of image A,  $cB$  is that of image B, and  $cA_h$  is that of haze in image A. Because

of residual errors in the geometric registration, some noise occurs after the processing of the haze approximation. Therefore,  $cA_h$  is smoothed using  $(3 \times 3)$  median filter. Then the approximation of haze is reconstructed with  $cA_h$  [Fig. 2(f)].

When the reconstructed haze is subtracted from the hazy image A, the final haze-free estimation is achieved [Fig. 2(c)]. The same wavelet analysis is applied to band 2 of the image.

MSS band 3 is a near-infrared channel. A systematic pattern of haze cannot be discerned in its image [Fig. 3(a)], which suggests that the scattering generated by particles in the atmosphere was very weak in

TABLE I  
MEAN VALUE OF THE DIFFERENT IMAGES AND HAZE

	Hazy 91	Haze-free86	Haze-off 91	Haze 91	Haze %
<b>Band 1</b>	23.3	19.5	19.6	3.7	15.9
<b>Band 2</b>	18.4	15.0	15.0	3.3	17.9
<b>Band 3</b>	53.0	53.4	53.0	0.0	0.0

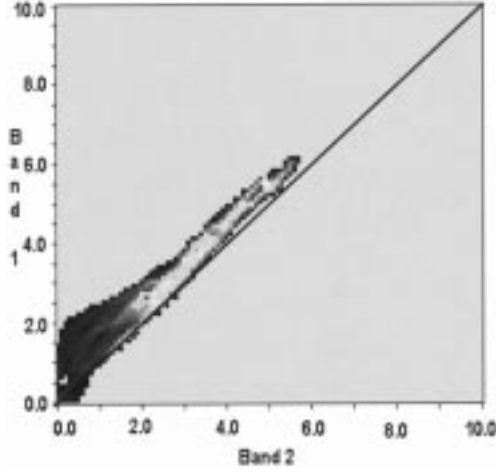


Fig. 5. Scatterplot between band 1 and band 2 of haze distributions, 1991 (in gray levels).

the near infrared. Images A and B are visually quite similar in band 3 [Fig. 3(a) and (b)], which supports the previous conclusion. In this case, we ignore the potential effect of haze in the final color composite reconstruction [Fig. 4(c)].

Visually comparing with original image A [Fig. 4(a)] and haze free image B [Fig. 4(b)] suggests that most haze has been successfully removed. The details of the image are preserved, however the accuracy of correction is difficult to assess by visual inspection alone.

To estimate the accuracy, we calculated the average gray levels of each band for all images (Table I). From Table I, the mean value of haze is only 15.9% of the total gray level in band 1 and 17.9% in band 2. It can also be seen that the mean values of band 3 of image A and B are quite similar, which indicates that band 3 does not need correction. When haze is removed from image A, the mean values in band 1 and 2 of the corrected images are very close to those of the haze-free image B (Table I). Fig. 5 shows the scatterplot between band 1 and band 2 of haze distribution subtracted from image (A). The haze in band 1 is about 10% higher than band 2, with a high agreement regarding the spatial distribution (correlation coefficient 0.91). Therefore, we conclude that the corrected results for the two bands are consistent and reasonable.

For definitive validation, the simultaneous ground and atmospheric measurements remain the optimum choice but this option is not available for our data set. As an alternative, to estimate the accuracy of the haze removal, we have selected some specific points, which temporally locate relatively stable urban areas (Fig. 6). This type of target has been recommended as generally invariant for change detection studies (i.e., [11], [18]). To avoid the effects of misregistration, we chose to average the gray levels of  $10 \times 10$  pixel windows. The differences between haze-off and haze-free means are less than 1 gray level in both bands 1 and 2 (Table II).

TABLE II  
THE DIGITAL VALUES (DV) OF THREE URBAN POSITIONS IN DIFFERENT IMAGES

	Hazy91	Haze-free86	Haze-off91	Haze 91	Haze%
<b>P1</b>					
band1	28.9	25.5	24.9	3.4	11.8
band2	26.9	25.3	24.9	1.9	7.1
<b>P2</b>					
band1	30.4	26.5	26.3	3.8	12.5
band2	29.1	27.0	26.1	2.3	7.9
<b>P3</b>					
band1	28.7	26.3	25.7	2.5	8.7
band2	27.9	26.2	25.9	1.9	6.8

## V. DISCUSSION AND CONCLUSIONS

Our proposed algorithm of the haze detection and removal with wavelet analysis (HAWAT) appears to effectively detect and remove haze over land targets. Although a low-haze or haze-free satellite image is needed as the reference (usually available in existing archives), the technique does not require coincident *in situ* measurements. If the low frequency distribution of land cover does not change substantially in the area of interest, even a mosaic image of the same area could be used as the reference as long as it is composed of clear scenes.

To extract the haze component from an image with wavelet analysis, the appropriate wavelet family should be selected, and the order of wavelet and the level of decomposition should be determined. The selection of a wavelet family is an involved mathematical problem that is not the focus of this paper. We selected the Daubechies wavelet family (*dbN*) because it produced a visually reasonable and flexible result and is commonly use for the decomposition of images. In our experiments, the result from the order 4 of the Daubechies wavelet was the best based on the visual inspection and calculated average estimation, so *db4* was selected for this study. The level of decomposition is critical to the result of haze removed. For example, if we chose the 0 level of decomposition after the difference between image A and B is subtracted from image A

$$\text{image } A' = \text{image } B \quad (4)$$

where image  $A'$  is the estimated corrected image A. In this case, the difference between A and B in land cover would be removed along with the haze. This is unacceptable for areas with dynamic high-frequency information content such as agricultural fields that exhibit significant seasonal variability. On the other hand, if level 10 were selected, which is the highest level for a  $2048 \times 2048$  image, then the haze distribution would be constant for the entire image

$$\text{image } A' = \text{image } B + \text{constant}. \quad (5)$$

All detail of the differences between image A and B would be preserved, with only the average value of the haze is removed. This is similar to conventional dark-object subtraction. It is easy to understand that the level of decomposition determines the balance between haze removal and the preservation of spatial detail. In this study, levels 4, 5, and 6 were tested with a final selection of level 5 based on visual inspection and calculated average estimation.

The essential conclusions of our HAWAT methodology are summarized as follows.

- 1) With the decomposition of an image using a wavelet transform, the spatially varying haze can be detected and removed. This

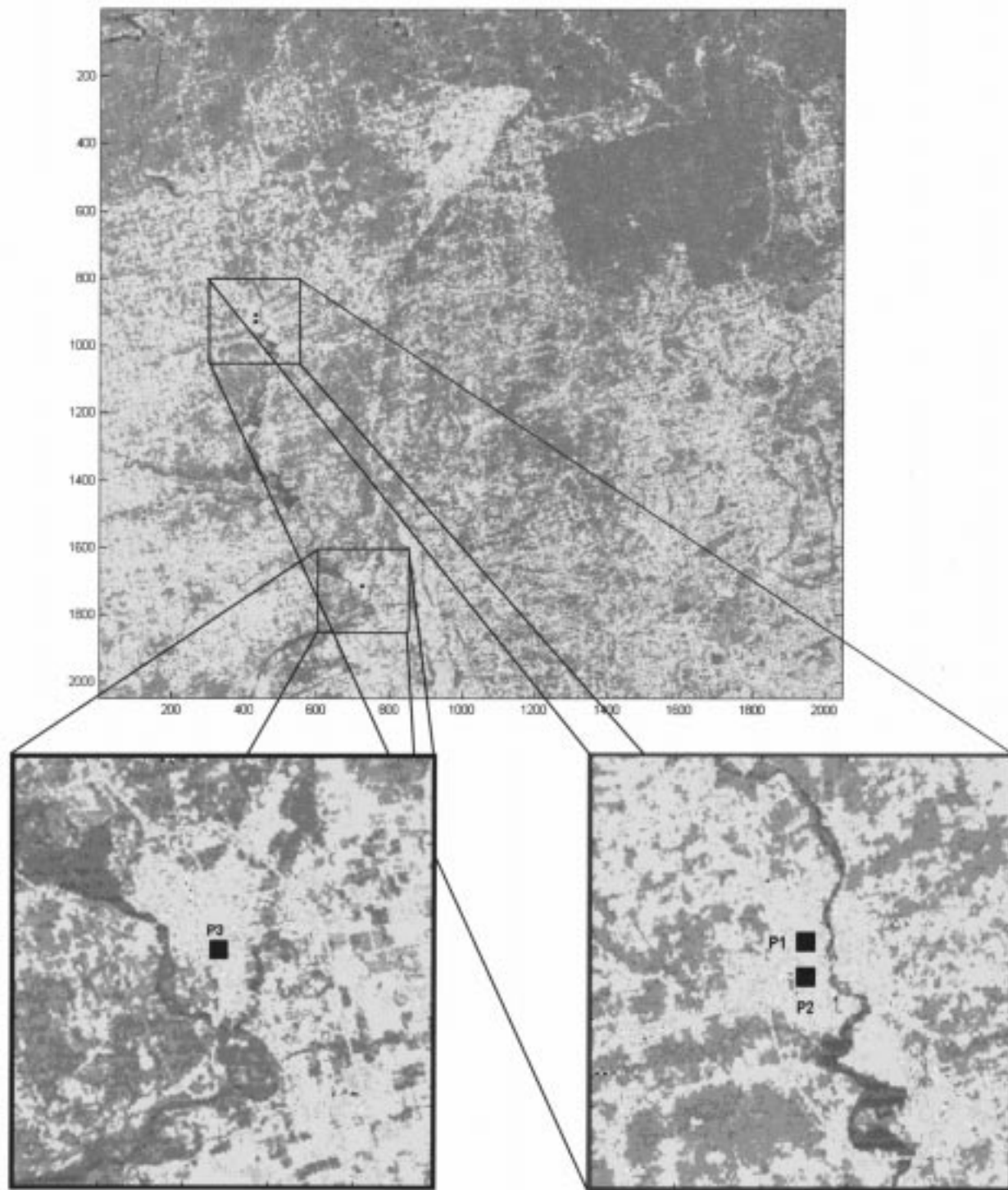


Fig. 6. Locations of checkpoints in the urban areas.

technique represents a substantial improvement over dark-object subtraction and other methods, which in most implementations assumes spatial invariance of haze.

- 2) Processing with HAWAT requires only information contained in image-based information, so it is practical and easy to use.
- 3) By its nature, our algorithm provides a correction procedure in the relative, not the absolute sense, which aims to remove the atmospheric effects in contaminated images relative to a reference image. Therefore, the average gray level values of the hazy image after correction should be similar to the reference image

in temporally stable areas. This provides a statistical indicator of quality.

- 4) The haze distributions of different bands can be subsequently combined to model and infer atmospheric parameters. This problem is currently under study.

The primary drawback of the HAWAT algorithm in its present form is the reliance on the operator's expertise in selecting of the decomposition level. Therefore, the development of automated wavelet analysis for haze detection and removal is being considered. The algorithm without reference image is also a further developing direction.



## ACKNOWLEDGMENT

The authors would like to thank the U.S. Environmental Protection Agency, National Exposure Research Laboratory, Environmental Sciences Division, Washington, DC, for the MSS images in this paper. They would also like to thank Dr. Phil. M. Teillet for his helpful suggestions and advice.

## REFERENCES

- [1] F. J. Ahern, R. J. Brown, J. Cihlar, R. P. Gauthier, J. Murphy, R. A. Neville, and P. M. Teillet, "Radiometric correction of visible and infrared remote sensing data at the Canada Centre for remote sensing," *Int. J. Remote Sensing*, vol. 8, pp. 1349–1376, 1987.
- [2] A. I. Anthis and A. P. Cracknell, "Use of satellite images for fog detection (AVHRR) and forecast of fog dissipation (METEOSAT) over lowland Thessalia, Hellas," *Int. J. Remote Sensing*, vol. 20, no. 6, pp. 1107–1124, 1999.
- [3] V. Caselles and M. J. Lopez Garcia, "An alternative simple approach to estimate atmospheric correction in multitemporal studies," *Int. J. Remote Sensing*, vol. 10, pp. 1127–1134, 1989.
- [4] P. S. Chavez, Jr., "An improved dark-object subtraction technique for atmospheric scattering correction of multispectral data," *Remote Sens. Environ.*, vol. 24, pp. 459–479, 1988.
- [5] J. Cihlar, Y. Du, and R. Latifovic, "Land cover dependence in the detection of contaminated pixels in satellite optical data," *IEEE Trans. Geosci. Remote Sensing*, vol. 39, pp. 1084–1094, May 2001.
- [6] A. Cohen, I. Daubechies, B. Jawerth, and P. Vial, "Multiresolution analysis, wavelets and fast wavelet transform on an interval," *CRAS Paris*, pp. 417–421, 1993.
- [7] I. Daubechies, "Orthonormal bases of compactly supported wavelets," *Commun. Pure Appl. Math.*, vol. 41, pp. 909–996, 1988.
- [8] —, "Ten lectures on wavelets," *SIAM*, p. 115, 132, 194, 242, 1992.
- [9] Y. Du and J. F. R. Gower, "Cloud detection and thin cloud calibration in NOAA AVHRR images with fuzzy logic," *Can. J. Remote Sensing*, vol. 26, pp. 54–63, Jan. 2000.
- [10] B. C. Forster, "Derivation of atmospheric correction procedures for Landsat MSS with particular reference to urban data," *Int. J. Remote Sensing*, vol. 5, no. 5, pp. 799–817, 1984.
- [11] F. G. Hall, D. E. Strebel, J. E. Nickeson, and S. J. Goetz, "Radiometric rectification: Toward a common radiometric response among multitemporal, multisensor images," *Remote Sens. Environ.*, vol. 35, pp. 11–27, 1991.
- [12] J. Lavreau, "De-haze landsat thematic mapper images," *Photogramm. Eng. Remote Sensing*, vol. 57, pp. 1297–1302, 1991.
- [13] R. S. Lunetta, L. G. Lyon, B. Guindon, and C. D. Elvidge, "North American landscape characterization dataset development and data fusion issues," *Photogramm. Eng. Remote Sensing*, vol. 64, no. 8, pp. 821–829, 1998.
- [14] J. Otterman and C. J. Robinove, "Effects of the atmosphere on the detection of surface changes from Landsat Multispectral Scanner data," *Int. J. Remote Sensing*, vol. 2, no. 4, pp. 351–360, 1981.
- [15] R. Richter, "A fast atmospheric correction algorithm applied to Landsat TM images," *Int. J. Remote Sensing*, vol. 11, no. 1, pp. 159–166, 1990.
- [16] —, "Atmospheric correction of satellite data with haze removal including a haze/clear transition region," *Comput. Geosci.*, vol. 22, no. 6, pp. 675–681, 1996.
- [17] —, "A spatially adaptive fast atmospheric correction algorithm," *Int. J. Remote Sensing*, vol. 17, no. 6, pp. 1201–1214, 1996.
- [18] J. R. Schott, C. Salvaggio, and W. J. Volchok, "Radiometric scene normalization using pseudoinvariant features," *Remote Sens. Environ.*, vol. 26, pp. 1–16, 1988.
- [19] M. A. Spanner, L. L. Pierce, D. L. Peterson, and S. W. Running, "Remote sensing of temperate coniferous forest leaf area index: The influence of canopy closure, understory vegetation and background reflectance," *Int. J. Remote Sensing*, vol. 11, no. 6, pp. 1469–1476, 1990.
- [20] S. G. Mallat, "Multifrequency channel decompositions of images and wavelet models," *IEEE Trans. Acoust., Speech, Signal Processing*, vol. 37, no. 12, pp. 2091–2110, 1989.
- [21] D. Tanre, C. Deroo, M. Duhaut, J. J. Morcrette, J. Perbos, and P. Y. Deschamps, "Description of a computer code to simulate the satellite signal in the solar spectrum: The 5S code," *Int. J. Remote Sensing*, vol. 11, no. 2, pp. 659–668, 1990.
- [22] P. M. Teillet and G. Fedosejevs, "On the dark target approach to atmospheric correction of remotely sensed data," *Can. J. Remote Sensing*, vol. 21, no. 4, pp. 374–387, 1995.
- [23] P. M. Teillet, "A status overview of earth observation calibration/validation for terrestrial applications," *Can. J. Remote Sensing*, vol. 23, no. 4, pp. 291–298, 1997.
- [24] R. K. Vincent, "An ERTS multispectral scanner experiment for mapping iron compounds," in *Proc. 8th Int. Symp. Remote Sensing of Environment*, Ann Arbor, MI, 1973, pp. 1239–1247.
- [25] C. Q. Zhu and X. M. Yang, "Study of remote sensing image texture analysis and classification using wavelet," *Int. J. Remote Sensing*, vol. 19, no. 16, pp. 3197–3203, 1998.

## Error Estimates for a Histogram in Scatterometer Geophysical Model Function Estimation

Maurizio Migliaccio and Paolo Colandrea

**Abstract**—The relationship between the normalized radar cross section  $\sigma^\circ$  and the ocean surface wind field, i.e., the geophysical model function, is a key element in scatterometry. Due to many unsolved physical modeling problems, only a semi-empirical approach can be used to quantitatively relate the observed  $\sigma^\circ$  to the wind field. Once the appropriate functional form has been selected, a model calibration procedure based on colocated  $\sigma^\circ$  measurements and external wind field observations/determinations is accomplished. To this end, a  $\sigma^\circ$  data grouping (binning) is performed to limit measurement uncertainties and reduce data volume. On this note, the binning procedure is revisited as an histogram estimation procedure and the relevant errors are determined. It is shown that in the best case of wind field error-free model the bias error introduced by the binning is negligible (but for low wind regimes) while the variance error is significant.

**Index Terms**—Data binning, geophysical model function, scatterometry.

### I. THEORY

IN THIS section, we provide the background theory to describe the binning procedure [1]–[5] as a histogram construction [6], and we introduce two natural error norms to evaluate the quality of the binning. For sake of simplicity we refer to  $\sigma^\circ$  as a function of the wind speed  $U$  only.<sup>1</sup>

The rationale of the approach can be summarized as follows. The  $\sigma^\circ$  is seen as a stochastic function of  $U$  whose probability density function (PDF)  $f(U)$  is meant to be estimated by means of its histogram. The quality of the procedure can be evaluated in terms of the true PDF.

Let us consider having  $M$  measurements at our disposal in our binning procedure and dividing the wind speed range of interest into bins of size  $\Delta U$ . For each bin we determine  $\hat{f}(U)$  as follows:

$$\hat{f}_m(U) = \frac{M_m}{M\Delta U} \quad \text{for} \quad U_m^{low} \leq U < U_m^{upp} \quad (1)$$

Manuscript received October 25, 2000; revised September 17, 2001.

M. Migliaccio is with the Università di Cagliari, Dipartimento di Ingegneria Elettrica ed Elettronica, 09123 Cagliari, Italy (e-mail: migliaccio@diee.unica.it).

P. Colandrea is with KELL Srl, 00193 Roma, Italy.  
Publisher Item Identifier S 0196-2892(02)01418-3.

<sup>1</sup>This can be the actual case in radar altimetry [2].